High-performance symmetric supercapacitor device based on carbonized iron-polyaniline/nickel graphene foam

M. N. Rantho, M. J. Madito and N. Manyala*

Department of Physics, Institute of Applied Materials, SARChI Chair in Carbon Technology and Materials, University of Pretoria 0028, South Africa.

*Corresponding author's email: ncholu.manyala@up.ac.za, Tel.: + (27)12 420 3549

HIGHLIGHTS

• C–Fe/PANI/Ni-GF was synthesized on nickel graphene foam by pyrolysis of the Fe-PANI mixture.

• The symmetric device was fabricated using C–Fe/PANI/Ni-GF electrode.

• The symmetric device exhibited high energy density and good long-term stability.

ABSTRACT

The carbonized iron-polyaniline/nickel graphene foam (C-Fe/PANI/Ni-GF) electrode was prepared by pasting a mixture of iron-polyaniline (Fe/PANI) on nickel graphene foam (Ni-GF) and carbonized under the nitrogen. For electrochemical characterization, the as-prepared electrode material was evaluated in both three and two-electrode (i.e. symmetric) cell configurations using 1 M NaNO$_3$ electrolyte. The symmetric device exhibited a maximum energy density of 68.0 W h kg^{-1} and power density of 718.2 W kg^{-1}, at a specific current of 1.0 A g^{-1} and the maximum potential of 1.7 V. The device further displayed long-term cycling stability with capacity retention of 91% over 10 000 galvanostatic charge-discharge cycles at 5 A g^{-1}. The stability of the device was also tested using the voltage holding and self-discharge approach whereby a slow-discharging process was observed, which suggests the practical application of the device.

KEYWORDS: Supercapacitor; Symmetric device; Negative electrode; PANI; Graphene foam

GRAPHICAL ABSTRACT
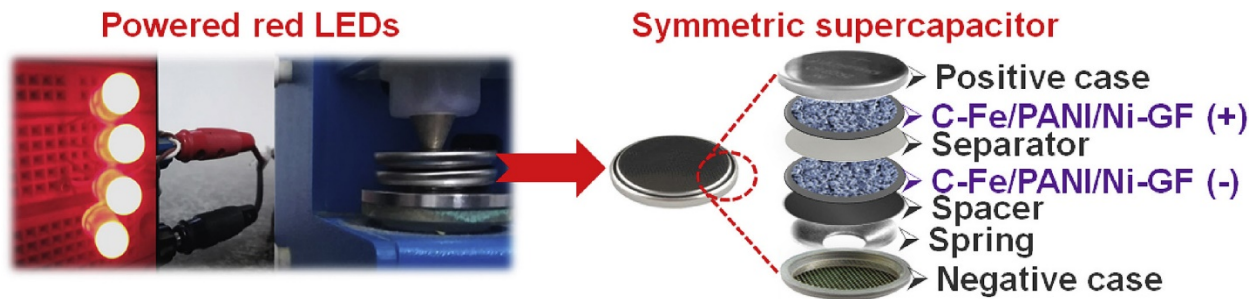
1. INTRODUCTION

Recently, there has been a demand for high-power performance, long cycle life, and enhanced safety energy-storage systems. In the view of the demands for energy-storage systems, supercapacitors (SCs) have received great attention due to their properties/electrochemical performance. SCs are high-power performance devices, and an extent of extensive research on SCs has been focusing on improving the energy density of SCs. In SCs, charges can be stored using three different mechanisms, viz., electric double-layer capacitors (EDLCs), pseudocapacitors or redox SCs and hybrid capacitors [1–3]. Asymmetric (hybrid) capacitors have been explored to increase the operating potential window to improve the energy density of the SCs [1–3]. Nowadays, ionic liquid electrolytes have been considered to provide the alternative improvement on SCs (high operating potential window) since they have a wider electrochemical stability window [4]. The main focus is also on developing hybrid SCs using the pseudocapacitive electrodes and battery-electrode materials since they exhibit high capacitance [5][6]. Therefore, both the high operating potential window and high capacitance of the pseudocapacitive electrodes and battery-electrode material significantly increase the energy density of the SCs while maintaining high power density. In addition, the development of the nanostructured materials has been explored to improve the rate capability of the battery-electrode materials.

In recent reports, conducting polymers are considered as pseudocapacitive materials suitable for the next generation of SCs [7–10]. Among these conducting polymers, polyaniline (PANI) has attractive properties, for instance, the morphological diversity, good redox reversibility, low cost, and simple synthesis [11]. The conducting polymers have a wide range of tunable properties since their conductivity is linked with the molecular structure, the level of doping and the

ordering of molecular packing [12–14]. It has been shown that PANI containing iron achieves high electrocatalytic and electrochemical performance with long-cycling stability [15–17]. Iron cations easily adsorb onto PANI due to functional groups of PANI which acts as active sites [18–21]. Available reports also show that the electrical conductivity of PANI can be enhanced by carbon nanotubes through π–π interactions [22,23]. However, compared to graphene the mass production of carbon nanotubes has a higher production cost hence graphene is preferred. Moreover, graphene has attracted great attention due to its remarkable properties, for instance, a high specific surface area, high electrical conductivity, and chemical stability [24–29]. Polymer/graphene interactions (nanocomposites) are expected to exhibit excellent electrochemical performance owing to a stronger π–π conjugation interactions and graphene properties. In fact, Yu et al. [30] have reported a remarkably high capacitance value of 1341 F g^{-1} for a PANI/3D graphene framework in an acidic electrolyte. Wang et al. [31], have demonstrated that the PANI/graphene nanocomposites show much better capacitance performance than that of individual PANI and the synergy effect of PANI and graphene greatly improves the retention life of the composite material. The key factors determining the electrochemical performances of the PANI/graphene nanocomposites, such as morphologies, synthesis methods, and synthesis conditions are detailed in the review titled: Polyaniline/graphene nanocomposites towards high-performance supercapacitors by Huang et al. [32].

This study reports on a high-performance symmetric supercapacitor based on the carbonized iron-polyaniline/nickel graphene foam electrode; prepared as shown in Scheme 1. The symmetric supercapacitor device was fabricated using 1 M NaNO$_3$ aqueous electrolyte. The C-Fe/PANI/Ni-GF symmetric device showed good electrochemical performance with a high energy density of 68.0 W h kg^{-1} and power density of 718.2 W kg^{-1}, at a specific current of 1.0 A g^{-1}; and excellent stability for both cycling and voltage holding stability test. The self-discharge approach was also used to test the stability of the device which showed a slow self-discharge process.

2. EXPERIMENTAL

2.1. Carbonization of an iron-polyaniline mixture on nickel graphene foam

The Fe-PANI mixture was synthesized as reported in our recent work [17]. Briefly, a 0.4 g of PANI and 0.2 g of iron nitrate nonahydrate (Fe(NO$_3$)$_3$·9H$_2$O) were dissolved in a 50 mL of ethanol and dispersed until the Fe-PANI slurry was formed. The slurry was pasted on graphene

supported by nickel foam and carbonized at 850 °C (ramp rate of 10 °C min^{-1}) for 2 h under nitrogen. After carbonization, the difference in the micrograph of the Ni-GF and that of Fe-PANI mixture on Ni-GF (C-Fe/PANI/Ni-GF) confirms a successful synthesis of the electrode which is expected to have strong metal-polymer/graphene interactions (see scheme 1). The as-prepared electrode material was used for both negative and positive electrode, respectively. For electrochemical characterization in three-electrode configuration, the Fe-PANI slurry was pasted on both sides of Ni-GF and after carbonization, the active material of the electrode had a mass of 2 mg. For the symmetric device fabrication, the slurry was only pasted on one side of Ni-GF and after carbonization; the electrode materials had masses of 1.5 mg (negative electrode) and 1.7 mg (positive electrode).
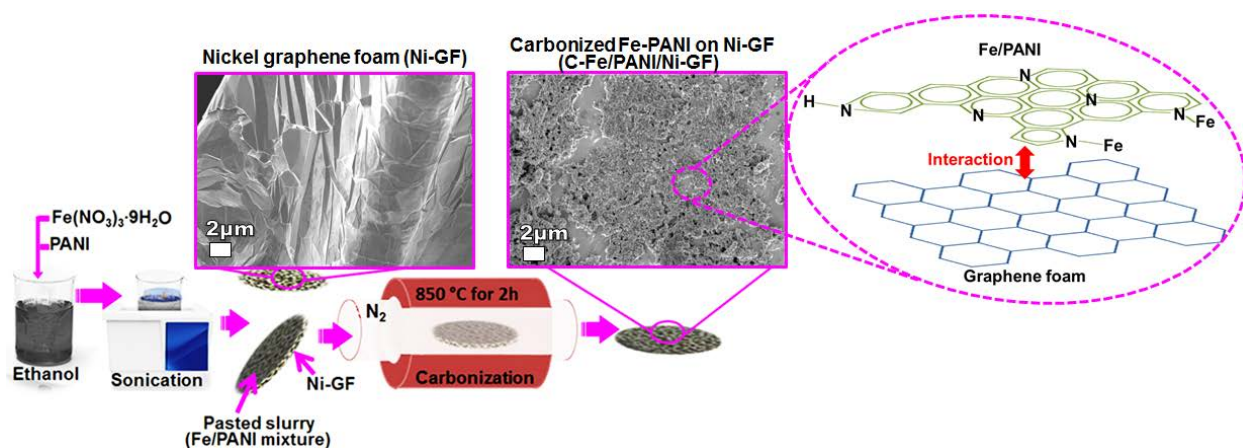
Scheme 1. The synthesis route for carbonized iron-polyaniline/nickel graphene foam electrode.

The Ni-GF was grown using atmospheric pressure chemical vapour deposition (AP-CVD). Graphene growth was carried out for 10 minutes at 1000 °C using a mixture of gasses, Ar: H$_2$: CH$_4$ with flow rates of 300: 200: 10 sccm, respectively. All the reagents used were purchased from Sigma Aldrich and a 3D scaffold template of polycrystalline nickel foam (Ni-F) from Alantum.

2.2. Morphological, composition and structural characterization

The C-Fe/PANI/Ni-GF material was characterized using scanning electron microscopy (SEM, Zeiss Ultra Plus 55 field emission scanning electron microscope), energy-dispersive X-ray spectrometer (EDS), high-resolution transmission electron microscopy (HR-TEM), X-ray

diffractometer (XRD, XPERTPRO diffractometer (PANalytical BV, Netherlands) and Raman spectroscopy. The HR-TEM analysis was carried out in a high-resolution transmission electron microscopy JEOL 2100 (from Tokyo Japan) equipped with LaB_6 filament, a Gartan U1000 camera of 2028 x 2028 pixels and was operated at 200 kV. The HR-TEM scanning transmission electron microscopy and the energy dispersive X-ray (STEM-EDX) were used for elemental distribution analysis. WITec alpha300 RAS+ confocal Raman microscope was used for Raman analysis/imaging. The analysis was carried out using a 532 nm laser and laser power of 5 mW. Raman image scans were acquired over 30×30 µm^2 area with 100 points per line and 100 lines per image using an integration time of 5 s. WITec project plus version software was used for Raman data processing.

2.3. Electrochemical characterization

A Biologic VMP-300 potentiostat (Knoxville TN 37,930, USA) was used for the electrochemical characterization. For three-electrode configuration, the measurements were carried out using three different neutral aqueous electrolytes, i.e. 1 M $NaNO_3$, $NaSO_4$ and $LiSO_4$ electrolyte. Cyclic voltammetry (CV) at scan rates of 5 to 100 mV s^{-1} and galvanostatic charge-discharge (GCD) were carried out for positive and negative electrode in the potential range of 0.0 to 0.7 V vs. Ag/AgCl and -1.0 to 0.0 V vs. Ag/AgCl. The electrochemical impedance spectroscopy (EIS) analysis was obtained using an open circuit over 10 mHz to 100 kHz. For two-electrode measurements, the symmetric device was fabricated using 1 M $NaNO_3$ aqueous electrolyte.

3. RESULTS AND DISCUSSION

3.1 Morphological, composition and structural characterization

The morphologies of the Ni-GF and C-Fe/PANI/Ni-GF samples were examined using SEM, as shown in figure 1(a) and 1(b), respectively. From the SEM images, the Ni-GF displays wrinkles and ripples of as-grown graphene [33]. The C-Fe/PANI/Ni-GF sample comprises of agglomerated nanograins; this is also shown in high magnification image in figure 1(c). The elemental composition of the C-Fe/PANI/Ni-GF was obtained using EDS and the maps are displayed in figure 1(d). Figure 1(d) shows the EDS maps of Ni, C, Fe, N, S, and O. Figure 1(e) shows the secondary electron beam image with an overlay combined image of the EDS maps of evaluated elements. These maps suggest that Fe cations are distributed homogeneously on the

PANI matrix in the C-Fe/PANI/Ni-GF electrode material. Figure 1(f) displays the average EDS spectrum which shows Fe, S, O, N, C, and Ni. A high content of Ni result from the Ni-GF substrate. The presence of S in the sample is from PANI synthesis, ammonium persulphate in particular, which degraded during pyrolysis. In addition, O and N are typically found in PANI. The XRD pattern obtained from the carbonized Fe/PANI (Figure S1), shows the diffraction peaks which matches Fe_3C, FeS, Fe and (002) graphitic plane.
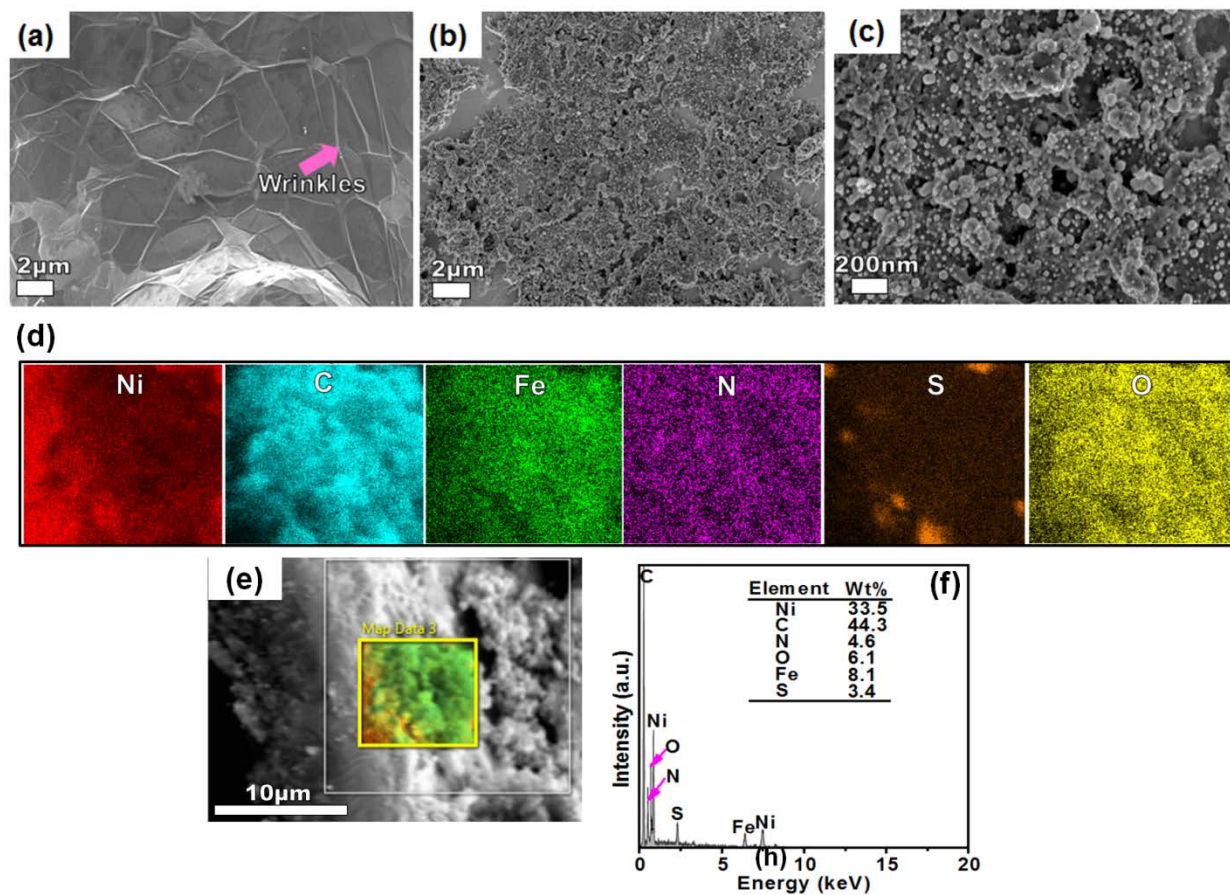

Figure 1. (a) SEM image of the Ni-GF and (b) C-Fe/PANI/Ni-GF. (c) The high magnification image of the C-Fe/PANI/Ni-GF. (d) The EDS maps of Ni, C, Fe, N, S, and O, and (e) the corresponding secondary electron beam image with an overlay combined image of the EDS maps of evaluated elements. (f) An average EDS spectrum.

Figure 2(a) and 2(b)-(c) show high-resolution TEM images of the as-synthesized C-Fe/PANI (without Ni foam) and C-Fe/PANI/Ni-GF, respectively. From these figures, C-Fe/PANI shows Fe cations attributed to Fe_3C, FeS and Fe anchored on PANI which has a sheet-like morphology. On the other hand, C-Fe/PANI/Ni-GF shows Fe/PANI on graphene foam (GF) which is grown on Ni substrate. In figure 2(c), GF shows a thickness of about 5 nm corresponding to few-layer

graphene. Furthermore, a scanning transmission electron microscopy along with energy dispersive X-ray maps are displayed in figure 2(d) and 2(e)-(j), respectively. The energy dispersive X-ray maps of the as-synthesized C-Fe/PANI/Ni-GF sample display the main elements of the sample (C, N, O, S, Fe and Ni) as seen from the EDS maps in figure 1.
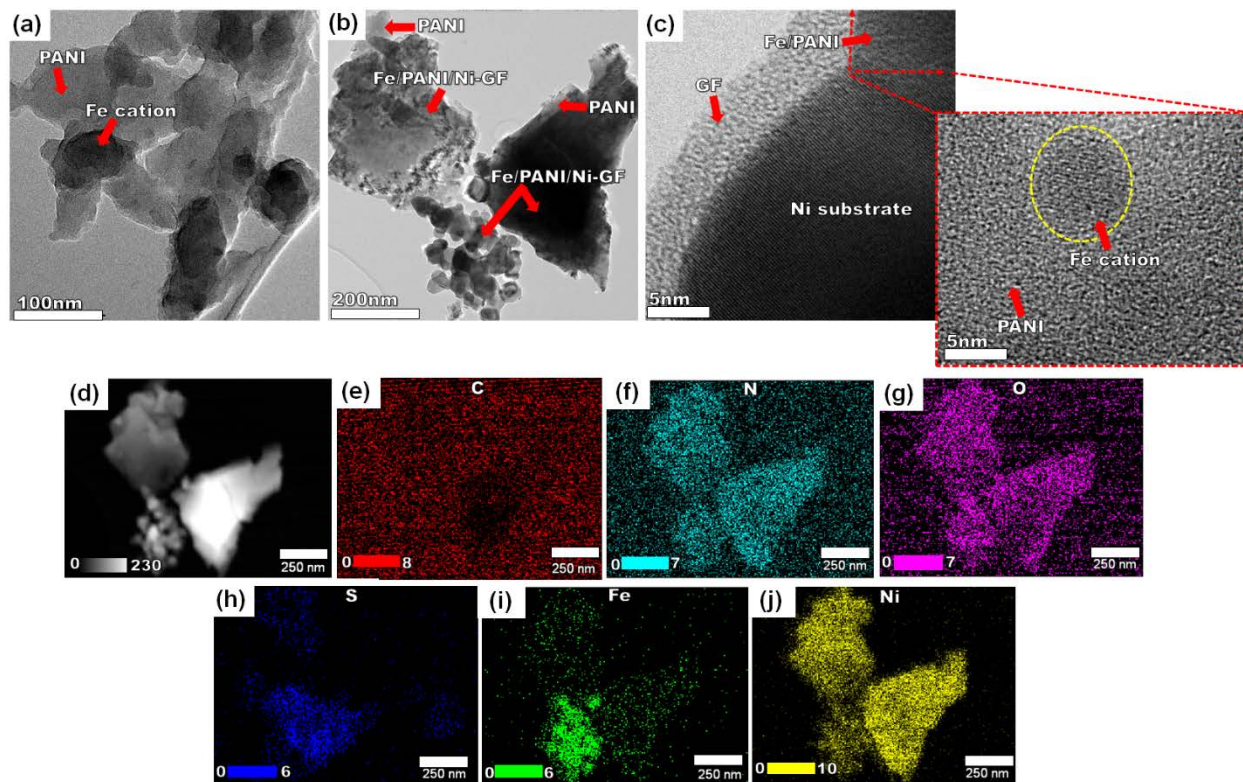

Figure 2. High-resolution TEM images: (a) As-synthesized C-Fe/PANI (without Ni foam), (b) and (c) C-Fe/PANI/Ni-GF. (d) Scanning transmission electron microscopy image and (e)-(j) the corresponding energy dispersive X-ray maps of C, N, O, S, Fe and Ni obtained from the as-synthesized C-Fe/PANI/Ni-GF sample.

Before pasting a slurry of Fe/PANI on the Ni-GF (see scheme 1), a Ni-GF was analyzed using Raman spectroscopy to investigate the quality and the number of graphene layers in the as-grown graphene. Figure 3(a-c) shows the Raman data of graphene on Ni foam. The main features of the Raman spectrum of graphene are the G-band (~1590 cm^{-1}), the 2D-band (~2690 cm^{-1}) and the D-band (disorder-induced band, 1350 cm^{-1}) [34–36]. In figure 3(a), the overlay image of the cluster analysis on the optical microscope image of the sample and the corresponding cluster average spectra (Figure 3(b)) reveals that the as-grown graphene has significant fractions of monolayer, bilayer and few-layer graphene (i.e. << 10 monolayers). Certainly, figure 3(b) shows the typical Raman spectrum of monolayer, bilayer and few-layer graphene with 2D-to-G peaks

intensity ratios of >2, ~1 and <0.6, respectively. In addition, the 2D peaks Full Width at Half Maximum (FWHM) for monolayer, bilayer and few-layer graphene are 30, 50 and 72 cm^{-1}, respectively, which demonstrate the characteristics of monolayer, bilayer and few-layer graphene. Briefly, the cluster analysis of the acquired Raman image data set automatically finds similar spectra in an image spectrum data set and creates the cluster distribution maps and the corresponding cluster average spectra. Furthermore, figure 3(c) shows the mapping of the D-to-G peaks intensities ratio. The map shows an average value of approximately zero confirming the zero intensity of the D-band in the Raman spectra which demonstrates high-quality graphene foam.

Figure 3(d-g) shows the Raman data of the C-Fe/PANI/Ni-GF. In figure 3(d), the overlay image of the cluster analysis on the optical microscope image and the corresponding cluster average spectra (Figure 3(e)) display typical Raman spectra of PANI (blue line) and graphene (green and pink line). From the overlay image in figure 3(d), the small areas of graphene suggest that the coating of the PANI on Ni-GF is not completely uniform across the substrate and that could be due to the porous nature of the Ni foam. Moreover, in figure 3(e), the D band (which is due to the functional groups of PANI [20,21]) in the spectra of graphene confirms the interaction/incorporation of the PANI functional groups in the graphene lattice. This is further confirmed by mapping of the D-to-G peaks intensities ratio, as shown in figure 3(f), which displays an average value of ~0.8. This confirms a high intensity of the D-band in the Raman spectra of the C-Fe/PANI/Ni-GF.

The Raman peaks in the range of 100 to 700 cm^{-1} are due to Fe–PANI, as shown in figure 3(g) and table 1. It is worth mentioning that the phases in figure 3(g) have X-ray diffraction peaks matching Inorganic Crystal Structure Database (ICSD) cards (α-S$_8$ ICSD #27261, α-FeOOH ICSD #77327, γ-FeOOH ICSD #93948, Fe$_2$O$_3$ ICSD #64599 and Fe$_3$O$_4$ ICSD #35000) which overlap with the diffraction peaks of the phases shown in the XRD data in figure S1.
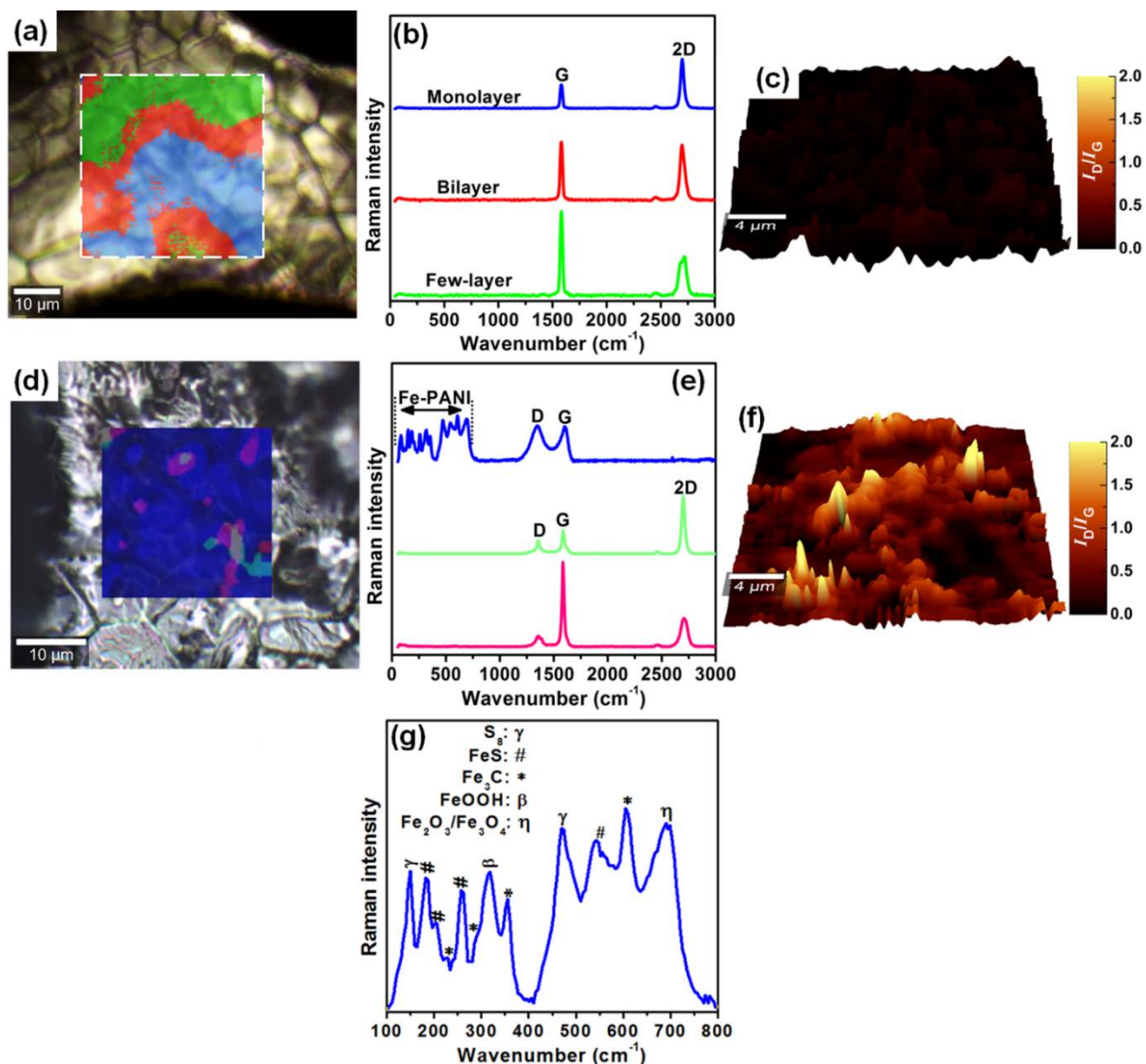
Figure 3. (a-c) Raman data of as-grown graphene on Ni foam (Ni-GF): (a) The optical microscope image with an overlay image of cluster analysis, and (b) the corresponding cluster average spectra (each spectrum-color correspond to the image area of the same color in (a)). (c) Mapping of the D-to-G peaks intensities ratio. (d-g) Raman data of C-Fe/PANI/Ni-GF: (d) The optical microscope image with an overlay image of cluster analysis, and (e) the corresponding cluster average spectra (each spectrum-color correspond to the image area of the same color in (d)). (f) Mapping of the D-to-G peaks intensities ratio. (g) The cluster average spectrum of the Fe-PANI range in (e).

Table 1. Raman peak positions of the Fe-PANI range in figure 3(g) of the C-Fe/PANI/Ni-GF and the corresponding phases.

Peak positions (cm^{-1})	Phases	Ref.
153	α-S$_8$	[37]
191	FeS	[38]
205	FeS	[38][39]
223	Fe$_3$C / α-S$_8$	[40][39]
265	FeS	[38][39]
290	Fe$_3$C / FeS	[40][39]
310	α-FeOOH	[41]
360	Fe$_3$C / γ-FeOOH	[40][39]
471	α-S$_8$	[37]
540	γ-FeOOH	[39]
603	Fe$_3$C	[40]
680	γ-Fe$_2$O$_3$/Fe$_3$O$_4$	[41][42]

In figure 4(a), the C 1s XPS core level spectrum of the C-Fe/PANI/Ni-GF shows different carbon compounds at 284.5 (C=C), 285.3 (C–C), 286.5 (C–OH/C–N), 287.6 (C–O–C) and 288.9 eV (C=O) attributed to the functional groups of PANI [43,44]. On the other hand, compared to the C-Fe/PANI/Ni-GF, the C 1s spectrum of the Ni-GF (Figure 4(b)) shows a predominant narrow peak of sp^2 C=C bond and relatively low-intensity peaks of the oxide components which could be due to surface-adsorbed CO_2 and O_2, and the $\pi-\pi^*$ electrons transition [45–47]; and this shows a form of high-quality graphene. Nonetheless, in the C-Fe/PANI/Ni-GF, the C 1s spectrum of the Ni-GF would be similar to that of the C-Fe/PANI/Ni-GF due to the interaction between the Fe/PANI and graphene foam during pyrolysis which is energetically favourable owing to the unpaired π-electron in graphene and the high electronegativity of oxygen present in PANI. The Fe 2p XPS core level spectrum of the C-Fe/PANI/Ni-GF (Figure 4(c)) shows fitted Fe 2p$_{3/2}$ binding energy peaks at 706.5 and 708.1eV attributed to Fe^0 (metallic Fe)/ Fe^{2+} and Fe^{3+} ions, respectively [48]. In figure 4(d), the N 1s core level spectrum shows characteristic nitrogen–carbon bond-related peaks which appears at 398.6 eV (pyridinic N), 400.2 eV (pyrrolic N), and 401.5 eV (graphitic N). A pyridinic N peak has the contribution of N–iron peak (399.3 eV) since the two peaks overlap [49]. The S 2p XPS core level spectrum shows peaks in the range of 160 – 65 eV attributed to the S^{2-} ions (160.7 and 161.9 eV fitted peaks of the S 2p$_{3/2}$ and S 2p$_{1/2}$ levels, respectively), S–C and/or S–S bonds (fitted peak at 163.3 eV of the S 2p$_{3/2}$ level). S 2p$_{1/2}$ fitted peak confirms a characteristic FeS bond-related peak which appears at 161.9 eV and in the S

2p$_{3/2}$ peak, S–C, S–S and S–S/S–C bonds have characteristic peaks at 163.2, 163.8, and 164.8 eV respectively [50].
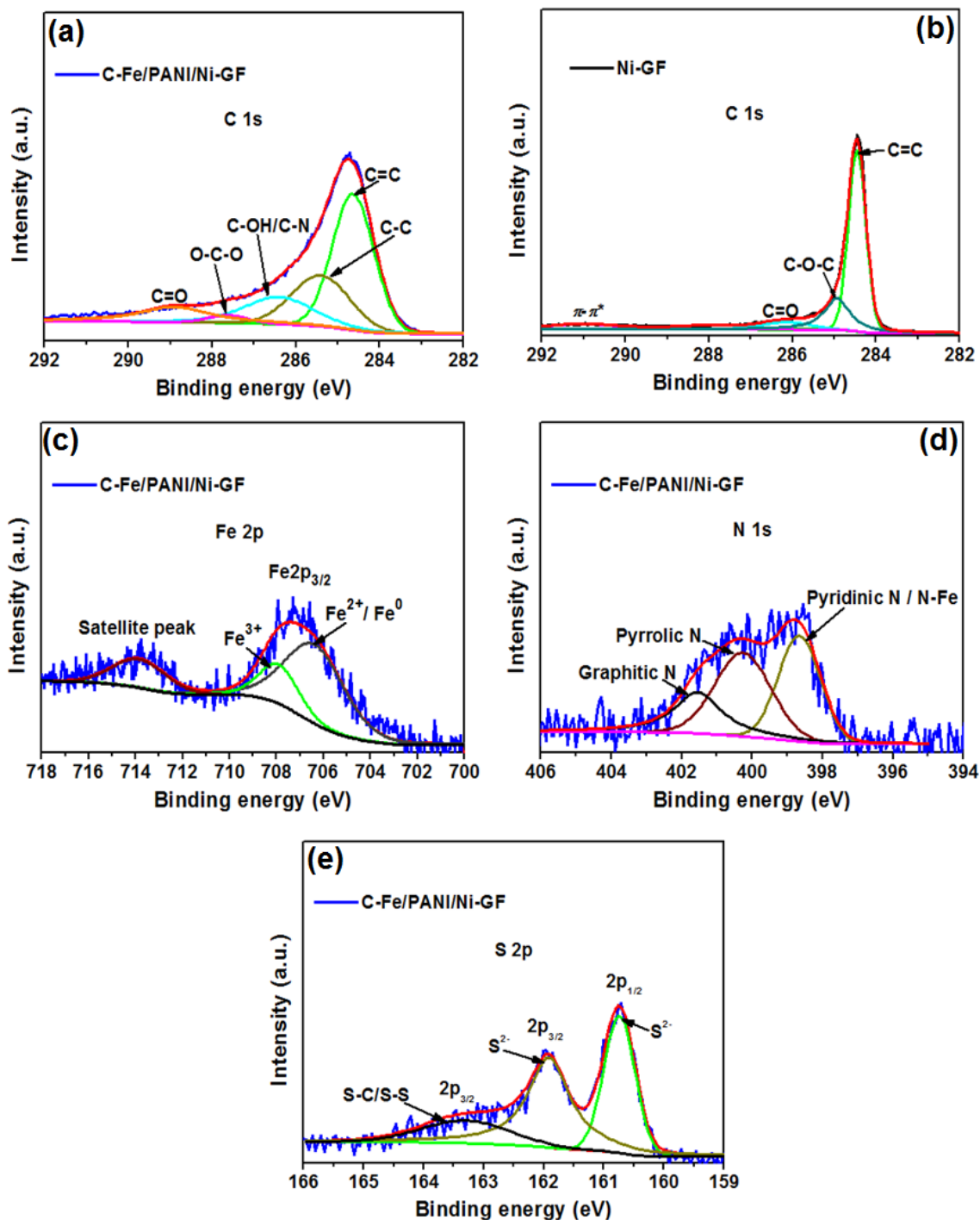

Figure 4. The XPS core level spectra: (a) C 1s of the C-Fe/PANI/Ni-GF and (b) Ni-GF; (c) Fe 2p, (d) N 1s, and (e) S 2p of the C-Fe/PANI/Ni-GF electrode material.

3.2 Electrochemical characterization

The as-prepared electrodes (C-Fe/PANI/Ni-GF) were evaluated as negative and positive electrodes using 1 M $NaNO_3$, $NaSO_4$ and $LiSO_4$ electrolyte in the three-electrode system, as shown in figure 5(a) and 5(b). The CV curves of the as-prepared electrode in both negative and positive potential window show pseudocapacitive behavior without obvious redox peaks. From figure 5, 1 M $NaNO_3$ electrolyte is the best electrolyte since it gives high current response compared to that of 1 M $NaSO_4$ and 1 M $LiSO_4$ electrolyte. This could be due to the small hydrated ion size of Na^+ (0.359 nm) and high ionic conductivity of 50.11 S cm^2 mol^{-1} compared to the Li^+ which has ion size of 0.381 nm and ionic conductivity of 38.69 S cm^2 mol^{-1} [51,52]. On the other hand, The accumulation of NO_3^- ions on the positive electrode might be higher than that of SO_4^{2-} ions since it has small hydrated ion size of 0.335 nm compared to 0.379 nm of the SO_4^{2-} ions [52]. It worth mentioning that the negative electrodes in 1 M $NaSO_4$ and 1 M $LiSO_4$ electrolyte could not reach a potential of 1.0 V vs. Ag/AgCl as the electrode in 1 M $NaNO_3$ electrolyte.
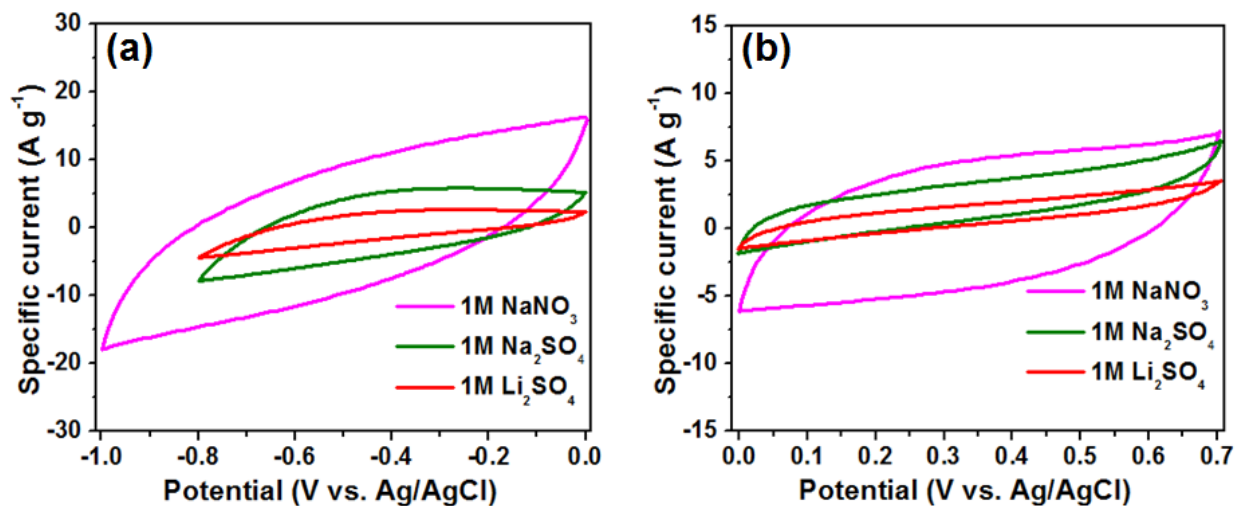

Figure 5. (a) and (b) Cyclic voltammetry curves of the as-prepared electrode at the scan rate of 50 mV s^{-1} in different aqueous electrolytes.

Based on the observation from figure 5, 1 M NaNO$_3$ electrolyte showed the best performance compared to the other electrolytes it was used for further electrochemical evaluation. The as-prepared electrode was further evaluated in the three electrode configuration using 1 M NaNO$_3$ electrolyte, as shown in figure S2(a-d). For as-prepared electrode the specific capacitance, C_S, was calculated for both positive and negative electrode (Figure S2(e)), from the GCD curves [3,53,54]:

$$C_S = \frac{I\Delta t}{m\Delta V} \tag{1}$$

where I/m is the specific current (A/g), m is the mass of the electrode material (g), Δt is the discharge time (s), and ΔV is the maximum potential.

From figure S2(e) it can be seen that in the positive potential window, the as-prepared electrode exhibited the high specific capacitance of 69.0 F g^{-1} at a specific current of 1 A g^{-1} and in the negative potential window it exhibits 139.9 F g^{-1}. For the as-prepared electrode, a symmetric supercapacitor device (scheme in figure 6(a)) was fabricated using 1 M NaNO$_3$ electrolyte; and the charge balance was done using equation S1 (supporting information). From the three-electrode measurements (Figure 6(b)), the as-prepared electrode in negative and positive potential window reaches -1.0 and 0.7 V vs. Ag/AgCl, respectively. Consequently, the symmetric device was able to reach the maximum potential of 1.7 V (Figure 6(c)). It can be seen from the CV curves of the device (Figure 6(c)) that it has a pseudocapacitive behavior; and these curves do not change with the increase in scan rate, which suggests that the device is stable. The GCD curves of the device shown in figure 6(d) at different specific currents in the range of 1 to 5 A g^{-1} which illustrates the pseudocapacitive behavior agreeing with the CV (Figure 6(c)). Moreover, because of the pseudocapacitive nature of the device, the specific capacity (Q_S) of the device (Figure 6(e)) was calculated using equation 2 [3,53–56]:

$$Q_S = \left(\frac{I}{m}\right)\frac{t}{3.6} \tag{2}$$

where I/m is the specific current (A/g), m is the mass of the electrode material (g), and t is the discharge time (s).

At a low specific current of 1 A g^{-1} the device exhibits a high specific capacity of 94.6 mA h g^{-1} which drops to 31.7 mA h g^{-1} at a high specific current of 5 A g^{-1}; such drop could be due to the limited time that ions have to access the surface of the electrode at high specific currents [57], and that could be due to the redox reactions (from the oxide phases present in the electrode) which limit the accessibility of the electrolyte ions. In addition, the observed drop in specific capacity values may be due to the increasing electronic field within the cell setup increased by an increase in the current density at a high cell potential window.
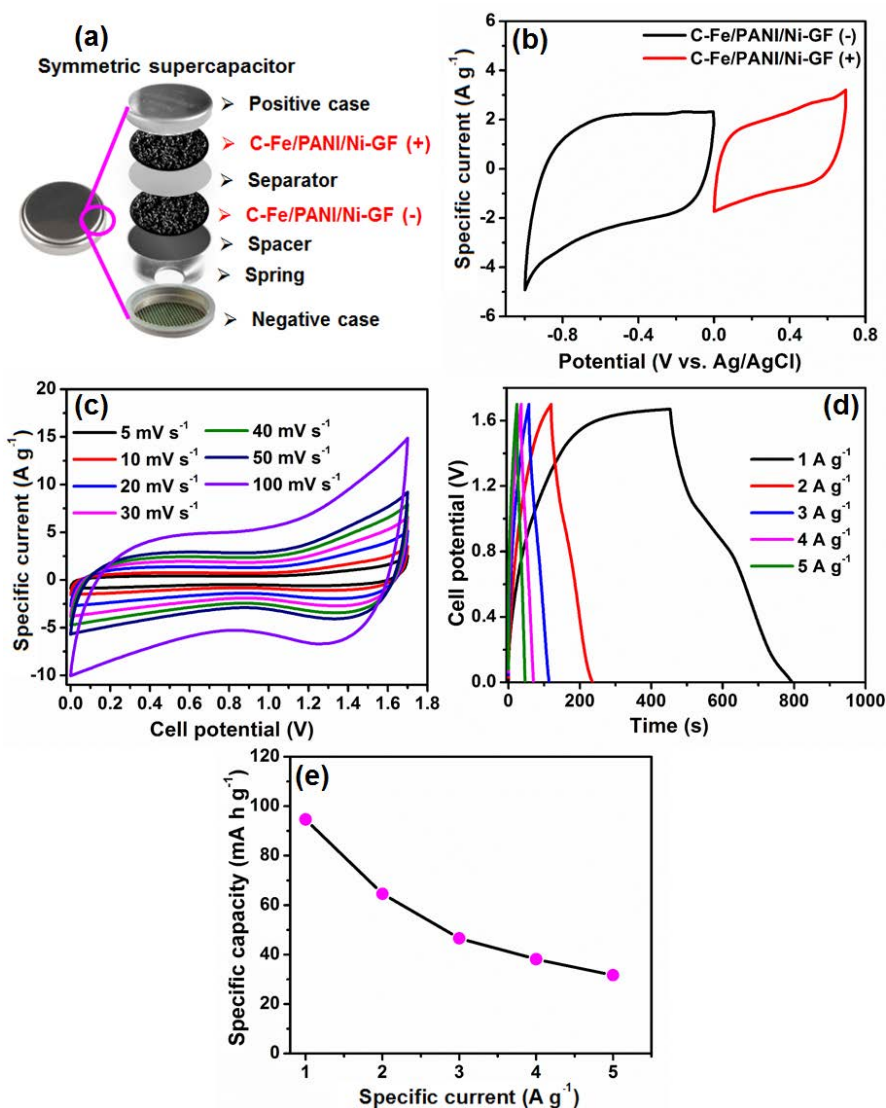

Figure 6. (a) Scheme of the fabricated device. (b) CV curves of the as-prepared electrode from the three-electrode measurements at 5 mV s^{-1}. (c) and (d) CV and GCD curves of the fabricated device, respectively. (e) Specific capacity versus specific current for the device.

The energy density, E_d and the power density, P_d were calculated using the GCD curves, as shown in figure 7(a), using equation 3 and 4, respectively:

$$E_d \ (\mathrm{W\,h\,kg^{-1}}) = \left(\frac{I}{m}\right)\frac{\int V(t)dt}{3.6} \tag{3}$$

$$P_d \ (\mathrm{W\,kg^{-1}}) = \frac{3.6\,E_d}{\Delta t} \tag{4}$$

where I/m is the specific current (A/g), $\int V(t)dt$ is the integral under the discharge curve and Δt is the discharge time (s).

The fabricated device displayed a maximum energy density of 68.0 W h kg^{-1} and power density of 718.2 W kg^{-1}, at a specific current of 1.0 A g^{-1}. At a high power density of 3843.0 W kg^{-1}, the energy density remained as high as 24.4 W h kg^{-1} at 5.0 A g^{-1}. Figure 7(b) shows the energy densities of the C-Fe/PANI (from our previous work [17]) and C-Fe/PANI/Ni-GF symmetric devices in the specific current range of 1.0 to 5.0 A g^{-1}. From the figure, the C-Fe/PANI/Ni-GF device shows higher energy density values compared to C-Fe/PANI device. Additionally, table 2 and the Ragone plot (Figure S3) also show that the energy and power densities for C-Fe/PANI/Ni-GF device are superior to those reported in the literature on PANI based symmetric devices. A high-performance of the C-Fe/PANI/Ni-GF device could be attributed to the synergy between Fe/PANI and graphene foam. Although the Ni-GF is well-recognized to possess high electrical conductivity compared to Ni foam, a high energy density exhibited by C-Fe/PANI/Ni-GF compared to C-Fe/PANI is mainly due to the synergistic effect of PANI and graphene and the contribution of the iron-composite layer. This is also reported in the literature that the PANI/graphene nanocomposites show much better capacitance performance than that of individual PANI and the synergy effect of PANI and graphene greatly improves the retention life of the composite material [30,31]. Also, studies have shown that iron-containing PANI, achieve high electrocatalytic performance and exhibit high cycling stability [58–60].
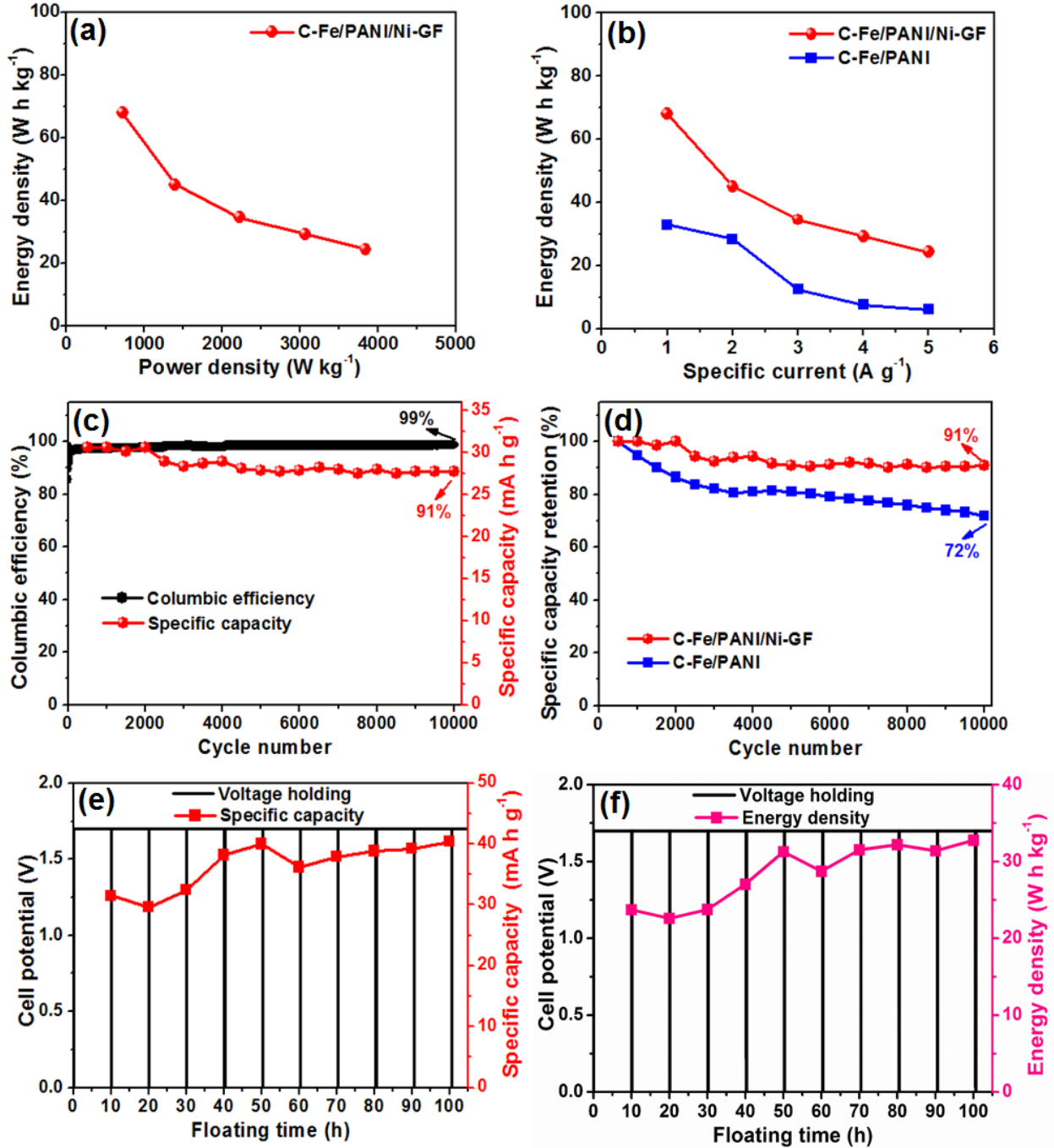
Figure 7. (a) Energy and power densities of the C-Fe/PANI/Ni-GF device. (b) Energy densities of the C-Fe/PANI and C-Fe/PANI/Ni-GF symmetric devices versus specific current. (c) The cycling stability test for the C-Fe/PANI/Ni-GF device at a specific current of 5 A g^{-1}. (d) The cycling stability results of the C-Fe/PANI and C-Fe/PANI/Ni-GF symmetric devices at a specific current of 5 A g^{-1}. (e) Voltage holding and specific capacity as a function of floating time at 5 A g^{-1}. (f) Voltage holding and energy density as a function of floating time at 5 A g^{-1}.

Table 2. Electrochemical performance comparison of PANI based symmetric devices.

Electrode device	Electrolyte	Specific current (A g^{-1})	Potential window (V)	Energy density (W h kg^{-1})	Power density (W kg^{-1})	Ref.
PANI	1 M H$_2$SO$_4$	1.0	1.0	23	180	M. Dirican et al. 2014 [61]
PANI/PCNF	1 M H$_2$SO$_4$	1.0	1.0	12	180	M. Dirican et al. 2014 [61]
PANI/MWNTs	1 M H$_2$SO$_4$	1 mA/cm^2	1.0	22	83	H. Mi et al. 2007 [62]
PANI/CNT	1 M H$_2$SO$_4$	0.5	0.8	7.11	201	K. Silas et al. 2016 [63]
C-Fe/PANI	6 M KOH	1.0	1.65	33.0	370.7	M.N. Rantho et al. 2018 [17]
C-Fe/PANI/Ni-GF	1 M NaNO$_3$	1.0	1.7	68.0	718.2	This work

Figure 7(c) shows the cycling stability test of the C-Fe/PANI/Ni-GF symmetric device performed at a specific current of 5.0 A g^{-1}. The cycling stability of the device exhibited a columbic efficiency of 99% and 91% capacity retention after a 10 000th galvanostatic charge-discharge cycle. In figure 7(d), the C-Fe/PANI/Ni-GF device shows a better cycling stability compared to C-Fe/PANI device [17], both performed at the same specific current of 5.0 A g^{-1}. This enhanced or long-cycling stability could also be due to the interactions between Fe/PANI and graphene foam. It is known that PANI–carbon (i.e., carbon nanotubes, nanofibers, graphene, etc.) based composites have long-cycling stability owing to the high stability of carbon [62,64–70]. The stability of the device was further tested via potentiostatic floating test (i.e. voltage holding) at 5.0 A g^{-1} and maximum operating potential of 1.7 V for 100 h, as shown in figure 7(e) and 7(f). Briefly, in voltage holding, a cell is kept at a specific fixed maximum operating potential for a long period of time, and the process includes a charge-discharge step for a few numbers of cycles in which the specific capacity of the device is monitored. Figure 7(e) and 7(f) show a significant increase in the specific capacity and energy density of the device after voltage

holding, and this could mean that the electrolyte ions access the electrodes pores more effectively after each holding period for intercalation into the electrode.

The electrical properties of the device before and after cycling stability, and after voltage holding were analyzed using EIS, as shown by the Nyquist plot in figure 8(a). In figure 8(a), the Nyquist plots do not show an obvious semi-circle in the high-frequency region (inset to the figure) demonstrating a lower electrode-electrolyte interface charge transfer resistance, R_{CT} hence a better capacitive behavior. The intersection of the Nyquist plots on the real component, Z' (see the inset to the figure), describes the equivalent series resistance, ESR or R_S, and the R_S values before stability ($R_S = 4.3\ \Omega$), after stability ($R_S = 5.5\ \Omega$) and after voltage holding ($R_S = 7.2\ \Omega$) are comparable suggesting good chemical stability of the device. A linear part of the plots (in the low-frequency) with angles greater than 45° deviates from an ideal capacitor. Furthermore, the Nyquist plot of the device was fitted (Figure 8(b)) using the equivalent circuit diagram shown in the insert to figure 8(b). The equivalent circuit diagram presents R_S in series with R_{CT}, and Warburg impedance characteristic element, W parallel to the real capacitance (Q_1) [71]. A deviation of the supercapacitor behavior from an ideal capacitive behavior is attributed to a leakage resistance, R_L (i.e. parallel to the mass capacitance, Q_2) [72,73].
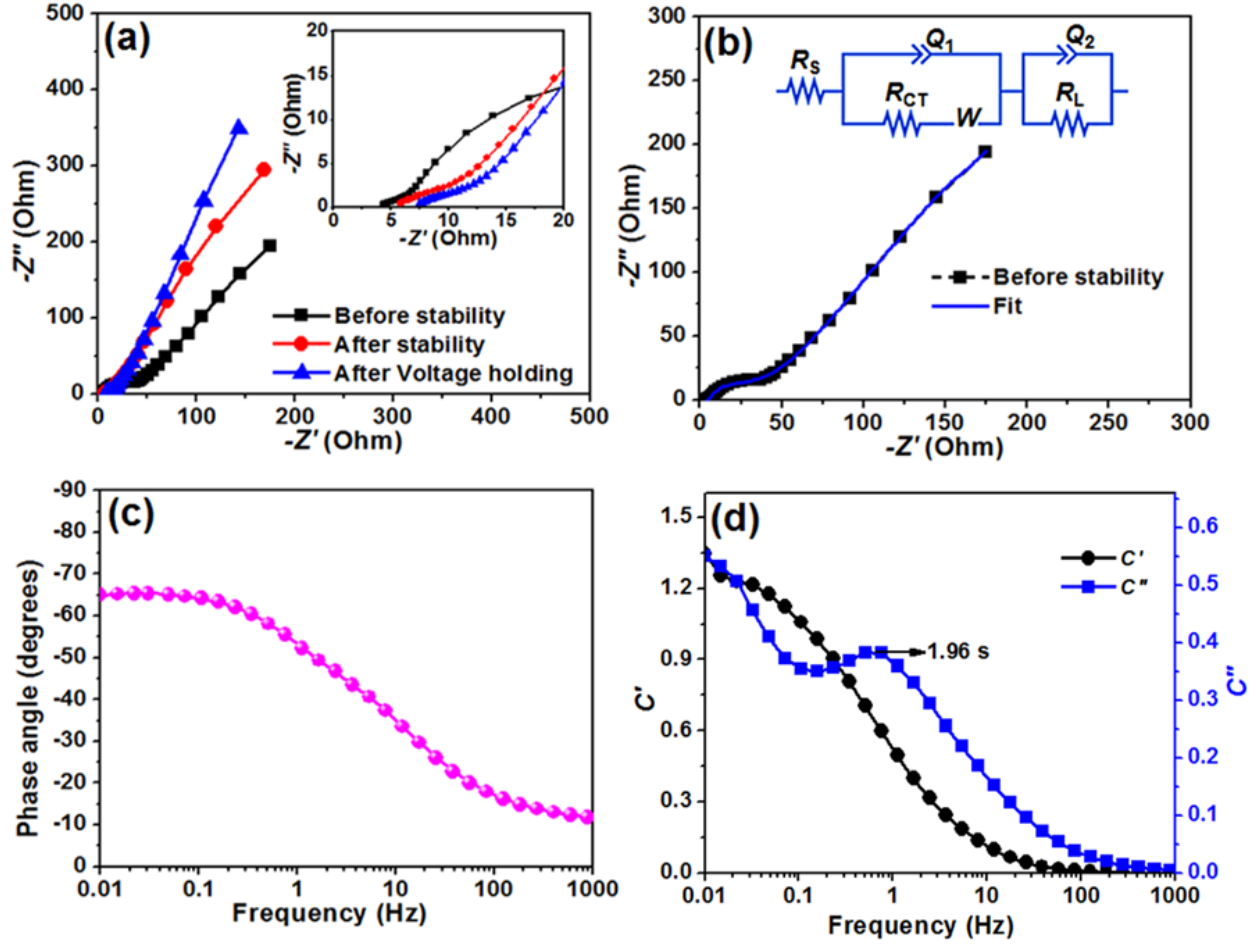
Figure 8. (a) Nyquist plots before stability, after stability and after voltage holding (the inset shows the enlarged high-frequency region). (b) The Nyquist plot and the fit (blue solid-line) of the equivalent circuit diagram in the insert. (c) The Bode plot. (d) The frequency dependence of the $C'(\omega)$ and $C''(\omega)$ capacitances.

Moreover, figure 8(c) displays the phase angle value of $-66°$ for the C-Fe/PANI/Ni-GF device. The frequency dependence of the $C'(\omega)$ and $C''(\omega)$ capacitances was calculated, as shown in figure 8(d), using the following expressions [74,75]:

The impedance, $Z(\omega)$ is expressed as

$$Z(\omega) = \frac{1}{j\omega \times C(\omega)} \qquad (5)$$

Therefore,

$$C'(\omega) = \frac{Z''(\omega)}{\omega|Z(\omega)|^2} \tag{6}$$

$$C''(\omega) = \frac{Z'(\omega)}{\omega|Z(\omega)|^2} \tag{7}$$

where Z' and Z'' are defined as

$$|Z(\omega)|^2 = Z'(\omega)^2 + Z''(\omega)^2 \tag{8}$$

and $\omega = 2\pi f$.

In figure 8(d), the $C'(\omega)$ which is the real accessible capacitance of the device that can be delivered corresponds to the deliverable capacitance of 1.35 F. The $C''(\omega)$ gives a relaxation time of 1.96 s which suggests that the device can be charged within few seconds.

Figure 9(a) shows a self-discharge curve of the device after it was fully charged (i.e. up to 1.7 V) at the constant specific current of 5 A g^{-1} and subjected to open circuit voltage to observe the behavior of the device. The device within the first 30 min of the self-discharge curve drops and maintains a potential of 1.27 V, and after 76 h, the device still maintains the potential of 0.85 V. This good performance of the device (a slow self-discharge process) is attributed to the pseudocapacitive behavior (slow discharging process) and high cycling stability of the electrode material as shown for both cycling and voltage holding stability test. However, there is quick cell potential drop from 1.7 to 1.4 V within the 2 min and this could be due to the decomposition of the solvent [76]. Briefly, the solvent can be reduced on the negative electrode when the cell is fully charged. Thus, the reduction can continue even after the cut-off of current, which leads to the fast decrease in the negative electrode potential. The self-discharge curve can be explained further by applying two models [77]: Model 1 relates the current leakage to the resistance, R of the supercapacitor:

$$V = V_0 e^{\left(-\frac{t}{RC}\right)} \tag{9}$$

where the device parameters, V_0, C and t are the initial potential, the equivalent capacity and the self-discharge period, respectively. The fitting of the self-discharge curve with this model is shown in figure 9(b), which gives a linear trend. It is worth noting that the cell potential in figure 9(b) is plotted on the logarithm scale.

Model 2 which is basically based on a diffusion control process is shown in figure 9(c). In this model, the stored ionic charges are lost during the discharging of the device and the cell potential is expressed by:

$$V = V_0 - mt^{\frac{1}{2}}$$

(10)

where the device parameters, m, V_0 and t are the ions diffusion parameter, initial potential and self-discharge period, respectively.

Both model 1 and 2 show a better fit to the self-discharge curve. This suggests that the self-discharge process of the device is influenced by both current leakage and diffusion control process.
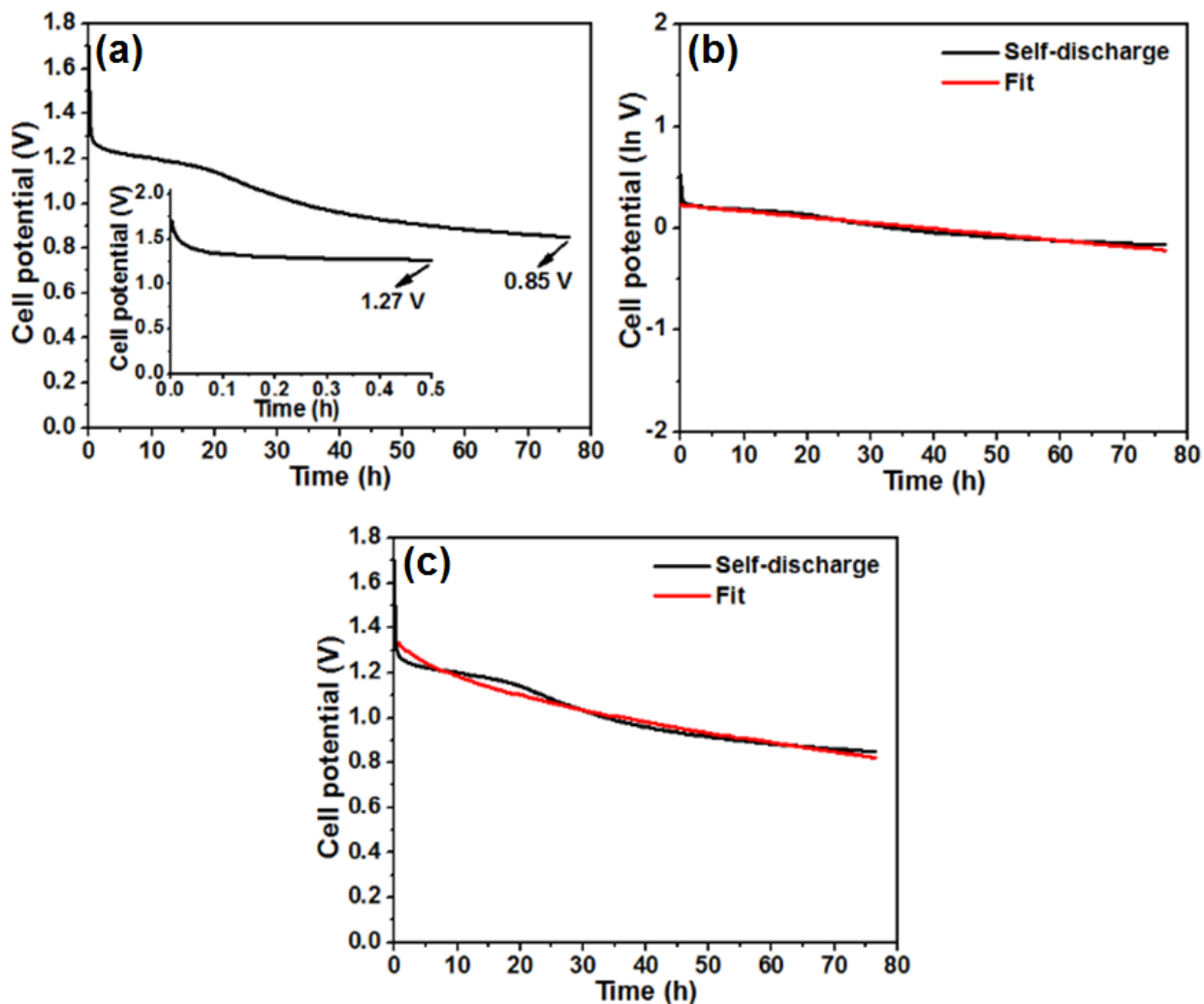
Figure 9. (a) Self-discharge curve of the C-Fe/PANI/Ni-GF symmetric capacitor after the device was fully charged to 1.7 V at constant specific current of 5 A g^{-1} (the inset figure shows the self-discharge curve within the first 30 min of the evaluation).(b) and (c) are the fitted self-discharge curves with equation (9) and (10), respectively.

Furthermore, the practical application of C-Fe/PANI/Ni-GF symmetric device was demonstrated, as shown in figure 10. This was demonstrated by powering four a red light emitting diodes (LEDs) of 1.8V and 30 mA each connected in parallel, as shown in figure 10(a). Two symmetric cells connected in series were charged to 1.7 V at a specific current of 2 A g^{-1}, thereafter, they were connected to LEDs. The change in the brightness of the LEDs is illustrated in figure 10(b). The red LEDs at 0 seconds displayed high brightness which decreases after 60 seconds. These attractive results demonstrate a potential energy-storage of the device, it can be fully charged in a short time and discharge slow.
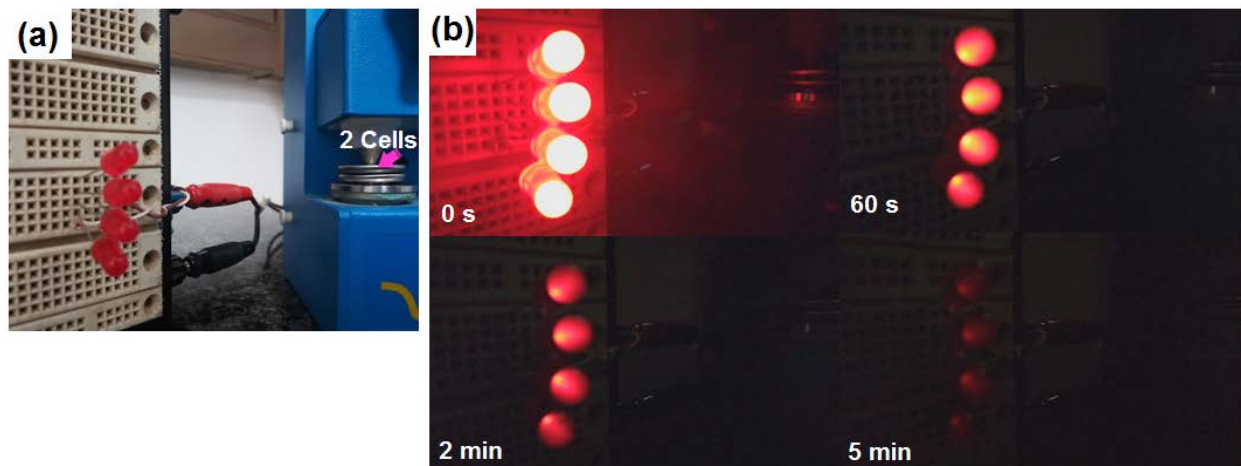
Figure 10. (a) The setup of the two devices in series and four red LEDs in parallel; and (b) powered red LEDs at different stages after the devices were fully charged to 1.7 V.

4. CONCLUSION

In this work, the nickel graphene foam (Ni-GF) was demonstrated to improve the electrochemical properties of the carbonized iron-polyaniline. We then successfully fabricated a symmetric supercapacitor device based on the carbonized iron-polyaniline/nickel graphene foam electrode using aqueous electrolyte. A fabricated symmetric device based on C-Fe/PANI/Ni-GF exhibited a maximum energy density of 68.0 W h kg^{-1} and power density of 718.2 W kg^{-1}, at a specific current of 1.0 A g^{-1} and cell potential window of 0.0 – 1.7 V. The device further displayed long-term cycling stability with capacity retention of 91% over 10 000 galvanostatic charge-discharge cycles at 5 A g^{-1}. The stability of the device was also tested using the voltage holding and self-discharge approach whereby a slow-discharging process was observed which suggests a practical application of the device. The enhanced capacitive performance and the long-cycling stability of the device are due to the synergy effect of Fe-PANI and graphene foam, thus making this electrode material suitable for high-performance supercapacitor applications. The electrochemical performance of the carbonized iron-polyaniline/nickel graphene foam electrode can be improved by varying morphologies, synthesis methods and conditions [32]; and

23

also by using ionic liquid electrolytes in the device to increase the potential window and hence the energy density.

ACKNOWLEDGMENTS

REFERENCES:

[1]   G. Zhang, M. Kong, Y. Yao, L. Long, M. Yan, One-pot synthesis of γ -MnS / reduced graphene oxide with enhanced performance for aqueous asymmetric supercapacitors, 065402 (n.d.). doi:10.1088/1361-6528/aa52a5.

[2]   G. Feng, S. Li, V. Presser, P.T. Cummings, Molecular Insights into Carbon Supercapacitors Based on Room-Temperature Ionic Liquids, J. Phys. Chem. Lett. 4 (2013) 3367–3376. doi:10.1021/jz4014163.

[3]   P. Simon, Y. Gogotsi, Materials for electrochemical capacitors, Nat. Mater. 7 (2008) 845–854.

[4]   T.Y. Kim, H.W. Lee, M. Stoller, D.R. Dreyer, C.W. Bielawski, R.S. Ruoff, K.S. Suh, High-Performance Supercapacitors Based on Poly(ionic liquid)-Modified Graphene Electrodes, (2010). doi:10.1021/NN101968P.

[5]   W. Zuo, R. Li, C. Zhou, Y. Li, J. Xia, J. Liu, Battery-Supercapacitor Hybrid Devices : *doi:10.1002/advs.201600539.

[6]   F. Wang, X. Wu, X. Yuan, Z. Liu, Latest advances in supercapacitors: From new electrode materials to novel device designs, Chem. Soc. Rev. 46 (2017) 6816–6854. doi:10.1039/c7cs00205j.

[7]   G. Wang, L. Zhang, J. Zhang, A review of electrode materials for electrochemical

supercapacitors, Chem. Soc. Rev. 41 (2012) 797–828. doi:10.1039/C1CS15060J.

[8]   K. Lota, V. Khomenko, E. Frackowiak, Capacitance properties of poly(3,4-ethylenedioxythiophene)/carbon nanotubes composites, J. Phys. Chem. Solids. 65 (2004) 295–301. doi:10.1016/J.JPCS.2003.10.051.

[9]   J.-Y. Kim, K.H. Kim, K.B. Kim, Fabrication and electrochemical properties of carbon nanotube/polypyrrole composite film electrodes with controlled pore size, J. Power Sources. 176 (2008) 396–402. doi:10.1016/J.JPOWSOUR.2007.09.117.

[10]   I. Shown, A. Ganguly, L.-C. Chen, K.-H. Chen, Conducting polymer-based flexible supercapacitor, Energy Sci. Eng. 3 (2015) 2–26. doi:10.1002/ese3.50.

[11]   X. Wang, J. Deng, X. Duan, D. Liu, J. Guo, P. Liu, Crosslinked polyaniline nanorods with improved electrochemical performance as electrode material for supercapacitors, J. Mater. Chem. A. 2 (2014) 12323. doi:10.1039/C4TA02231A.

[12]   G. Giri, E. Verploegen, S.C.B. Mannsfeld, S. Atahan-Evrenk, D.H. Kim, S.Y. Lee, H.A. Becerril, A. Aspuru-Guzik, M.F. Toney, Z. Bao, Tuning charge transport in solution-sheared organic semiconductors using lattice strain, Nature. 480 (2011) 504–508. doi:10.1038/nature10683.

[13]   G. Sabouraud, S. Sadki, N. Brodie, Guillaume Sabouraud, The mechanisms of pyrrole electropolymerization, Chem. Soc. Rev. 29 (2000) 283–293. doi:10.1039/a807124a.

[14]   D. Li, J. Huang, R.B. Kaner, Polyaniline Nanofibers: A Unique Polymer Nanostructure for Versatile Applications, Acc. Chem. Res. 42 (2009) 135–145. doi:10.1021/ar800080n.

[15]   H. Mi, X. Zhang, X. Ye, S. Yang, Preparation and enhanced capacitance of core–shell polypyrrole/ polyaniline composite electrode for supercapacitors, J. Power Sources. 176 (2008) 403–409. doi:10.1016/j.jpowsour.2007.10.070.

[16]   C. Portet, P.L. Taberna, P. Simon, E. Flahaut, C. Laberty-Robert, High power density electrodes for Carbon supercapacitor applications, Electrochim. Acta. 50 (2005) 4174–4181. doi:10.1016/j.electacta.2005.01.038.

[17] M.N. Rantho, M.J. Madito, N. Manyala, Symmetric supercapacitor with supercapattery behavior based on carbonized iron cations adsorbed onto polyaniline, Electrochim. Acta. 262 (2018). doi:10.1016/j.electacta.2018.01.001.

[18] B. Yanwu Zhu, S. Murali, W. Cai, X. Li, J. Won Suk, J.R. Potts, R.S. Ruoff, Y. Zhu, S. Murali, W. Cai, X. Li, J.W. Suk, J.R. Potts, R.S. Ruoff, Graphene and Graphene Oxide: Synthesis, Properties, and Applications, (n.d.). doi:10.1002/adma.201001068.

[19] Removal of Aqueous Hg(II) by Polyaniline: Sorption Characteristics and Mechanisms, (n.d.). doi:10.1021/es803710k.

[20] J. Zhang, C. Liu, G. Shi, Raman spectroscopic study on the structural changes of polyaniline during heating and cooling processes, J. Appl. Polym. Sci. 96 (2005) 732–739. doi:10.1002/app.21520.

[21] M. Sawangphruk, M. Suksomboon, K. Kongsupornsak, J. Khuntilo, P. Srimuk, Y. Sanguansak, P. Klunbud, P. Suktha, P. Chiochan, High-performance supercapacitors based on silver nanoparticle–polyaniline–graphene nanocomposites coated on flexible carbon fiber paper, J. Mater. Chem. A. 1 (2013) 9630. doi:10.1039/c3ta12194a.

[22] Q. Yao, L. Chen, W. Zhang, S. Liufu, X. Chen, Enhanced Thermoelectric Performance of Single-Walled Carbon Nanotubes/Polyaniline Hybrid Nanocomposites, ACS Nano. 4 (2010) 2445–2451. doi:10.1021/nn1002562.

[23] Q. Wang, Q. Yao, J. Chang, L. Chen, Enhanced thermoelectric properties of CNT/PANI composite nanofibers by highly orienting the arrangement of polymer chains, J. Mater. Chem. 22 (2012) 17612. doi:10.1039/c2jm32750c.

[24] H. Huang, J. Zhang, L. Jiang, Z. Zang, Preparation of cubic Cu2O nanoparticles wrapped by reduced graphene oxide for the efficient removal of rhodamine B, J. Alloys Compd. 718 (2017) 112–115. doi:10.1016/j.jallcom.2017.05.132.

[25] X. Liu, T. Xu, Y. Li, Z. Zang, X. Peng, H. Wei, W. Zha, F. Wang, Enhanced X-ray photon response in solution-synthesized CsPbBr 3 nanoparticles wrapped by reduced graphene oxide, Sol. Energy Mater. Sol. Cells. (2018). doi:10.1016/j.solmat.2018.08.009.

[26] C. Lee, X. Wei, J.W. Kysar, J. Hone, of Monolayer Graphene, (2008).

[27] B.Z.J.Æ.A. Zhamu, Processing of nanographene platelets (NGPs) and NGP nanocomposites : a review, (2008) 5092–5101. doi:10.1007/s10853-008-2755-2.

[28] M.J. Madito, A. Bello, J.K. Dangbegnon, C.J. Oliphant, W.A. Jordaan, D.Y. Momodu, T.M. Masikhwa, F. Barzegar, M. Fabiane, N. Manyala, atmospheric pressure chemical vapour deposition A dilute Cu (Ni) alloy for synthesis of large-area Bernal stacked bilayer graphene using atmospheric pressure chemical vapour deposition, 015306 (2016). doi:10.1063/1.4939648.

[29] K. S. Novoselov, A. K. Geim, S. V. Morozov, D. Jiang, Y. Zhang, S. V. Dubonos, I. V. Grigorieva, A. A. Firsov, Electric Field Effect in Atomically Thin Carbon Films, Science, 666 (2004) 666-669. doi:10.1126/science.1102896 .

[30] M. Yu, Y. Huang, C. Li, Y. Zeng, W. Wang, Y. Li, P. Fang, X. Lu, Y. Tong, Building Three-Dimensional Graphene Frameworks for Energy Storage and Catalysis, Adv. Funct. Mater. 25 (2015) 324–330. doi:10.1002/adfm.201402964.

[31] H. Wang, Q. Hao, X. Yang, L. Lu, X. Wang, A nanostructured graphene/polyaniline hybrid material for supercapacitors, Nanoscale. 2 (2010) 2164. doi:10.1039/c0nr00224k.

[32] Z. Huang, L. Li, Y. Wang, C. Zhang, T. Liu, Polyaniline/graphene nanocomposites towards high-performance supercapacitors: A review, Compos. Commun. 8 (2018) 83–91. doi:10.1016/J.COCO.2017.11.005.

[33] C. Mattevi, H. Kim, M. Chhowalla, A review of chemical vapour deposition of graphene on copper, J. Mater. Chem. 21 (2011) 3324.

[34] Y. Zhang, T. Tang, C. Girit, Z. Hao, M.C. Martin, A. Zettl, M.F. Crommie, Y.R. Shen, F. Wang, Direct observation of a widely tunable bandgap in bilayer graphene, Nature. 459 (2009) 820–3.

[35] W. Fang, A.L. Hsu, R. Caudillo, Y. Song, A.G. Birdwell, E. Zakar, M. Kalbac, M. Dubey, T. Palacios, M.S. Dresselhaus, P.T. Araujo, J. Kong, Rapid identification of stacking orientation in isotopically labeled chemical-vapor grown bilayer graphene by Raman

spectroscopy, Nano Lett. 13 (2013) 1541–1548.

[36] M.J. Madito, A. Bello, J.K. Dangbegnon, C.J. Oliphant, W.A. Jordaan, T.M. Masikhwa, D.Y. Momodu, N. Manyala, Raman analysis of bilayer graphene film prepared on commercial Cu(0.5 at% Ni) foil, J. Raman Spectrosc. (2015). doi:10.1002/jrs.4848.

[37] C. Avril, V. Malavergne, R. Caracas, B. Zanda, B. Reynard, E. Charon, E. Bobocioiu, F. Brunet, S. Borensztajn, S. Pont, M. Tarrida, F. Guyot, Raman spectroscopic properties and Raman identification of CaS-MgS-MnS-FeS-Cr $_2$ FeS $_4$ sulfides in meteorites and reduced sulfur-rich systems, Meteorit. Planet. Sci. 48 (2013) 1415–1426. doi:10.1111/maps.12145.

[38] G. Genchev, A. Erbe, Raman Spectroscopy of Mackinawite FeS in Anodic Iron Sulfide Corrosion Products, J. Electrochem. Soc. 163 (2016) C333–C338. doi:10.1149/2.1151606jes.

[39] J.-A. Bourdoiseau, M. Jeannin, R. Sabot, C. Rémazeilles, P. Refait, Characterisation of mackinawite by Raman spectroscopy: Effects of crystallisation, drying and oxidation, Corros. Sci. 50 (2008) 3247–3255. doi:10.1016/J.CORSCI.2008.08.041.

[40] X. Yang, C. Li, J. Huang, Y. Liu, W. Chen, J. Shen, Y. Zhu, C. Li, Nitrogen-doped Fe $_3$ C@C particles as an efficient heterogeneous photo-assisted Fenton catalyst, RSC Adv. 7 (2017) 15168–15175. doi:10.1039/C7RA00486A.

[41] P. Colomban, S. Cherifi, G. Despert, Raman identification of corrosion products on automotive galvanized steel sheets, J. Raman Spectrosc. 39 (2008) 881–886. doi:10.1002/jrs.1927.

[42] M.K. Nieuwoudt, J.D. Comins, I. Cukrowski, The growth of the passive film on iron in 0.05 M NaOH studied in situ by Raman micro-spectroscopy and electrochemical polarisation. Part I: near-resonance enhancement of the Raman spectra of iron oxide and oxyhydroxide compounds, J. Raman Spectrosc. 42 (2011) 1335–1339. doi:10.1002/jrs.2837.

[43] X. Feng, Z. Yan, N. Chen, Y. Zhang, X. Liu, Y. Ma, X. Yang, W. Hou, Synthesis of a graphene/polyaniline/MCM-41 nanocomposite and its application as a supercapacitor,

New J. Chem. 37 (2013) 2203. doi:10.1039/c3nj00108c.

[44]   S.K. Lai, C.M. Luk, L. Tang, K.S. Teng, S.P. Lau, Photoresponse of polyaniline-functionalized graphene quantum dots, Nanoscale. 7 (2015) 5338–5343. doi:10.1039/C4NR07565J.

[45]   H. Aoki, M. S. Dresselhaus, eds., Physics of Graphene, Springer, New York, 2014.

[46]   M. Hsiao, S. Liao, M. Yen, C. Teng, S. Lee, N. Pu, C. Wang, Y. Sung, M. Ger, C. Ma, M. Hsiao, Preparation and properties of a graphene reinforced nanocomposite conducting plate, J. Mater. Chem. 20 (2010) 8496.

[47]   S. Ogawa, T. Yamada, S. Ishidzuka, A. Yoshigoe, M. Hasegawa, Y. Teraoka, Y. Takakuwa, Graphene Growth and Carbon Diffusion Process during Vacuum Heating on Cu (111)/ Al 2 O 3 Substrates, Jpn. J. Appl. Phys. 52 (2013) 110122.

[48]   G.H. Le, A.Q. Ha, Q.K. Nguyen, K.T. Nguyen, P.T. Dang, H.T.K. Tran, L.D. Vu, T. V Nguyen, G.D. Lee, T.A. Vu, Removal of Cd $^{2+}$ and Cu $^{2+}$ ions from aqueous solution by using Fe–Fe $_3$ O $_4$ /graphene oxide as a novel and efficient adsorbent, Mater. Res. Express. 3 (2016) 105603. doi:10.1088/2053-1591/3/10/105603.

[49]   G. Wu, C.M. Johnston, N.H. Mack, K. Artyushkova, M. Ferrandon, M. Nelson, J.S. Lezama-Pacheco, S.D. Conradson, K.L. More, D.J. Myers, P. Zelenay, Synthesis–structure–performance correlation for polyaniline–Me–C non-precious metal cathode catalysts for oxygen reduction in fuel cells, J. Mater. Chem. 21 (2011) 11392. doi:10.1039/c0jm03613g.

[50]   M.V. Morales-Gallardo, A.M. Ayala, M. Pal, M.A. Cortes Jacome, J.A. Toledo Antonio, N.R. Mathews, Synthesis of pyrite FeS2 nanorods by simple hydrothermal method and its photocatalytic activity, Chem. Phys. Lett. 660 (2016) 93–98. doi:10.1016/J.CPLETT.2016.07.046.

[51]   A.G. Volkov, S. Paula, D.W. Deamer, Two mechanisms of permeation of small neutral molecules and hydrated ions across phospholipid bilayers, Bioelectrochemistry Bioenerg. 42 (1997) 153–160. doi:10.1016/S0302-4598(96)05097-0.

[52]   Sept, PHENOMENOLOGICAL THEORY OF ION SOLVATION, (1959). https://pubs.acs.org/doi/pdf/10.1021/j150579a011 (accessed March 8, 2018).

[53]   B. Akinwolemiwa, C. Peng, G.Z. Chen, Redox electrolytes in supercapacitors, J. Electrochem. Soc. 162 (2015) A5054–A5059. doi:10.1149/2.0111505jes.

[54]   A. Laheäär, P. Przygocki, Q. Abbas, F. Béguin, Appropriate methods for evaluating the efficiency and capacitive behavior of different types of supercapacitors, 2015. doi:10.1016/j.elecom.2015.07.022.

[55]   K.O. Oyedotun, M.J. Madito, A. Bello, D.Y. Momodu, A.A. Mirghni, N. Manyala, Investigation of graphene oxide nanogel and carbon nanorods as electrode for electrochemical supercapacitor, Electrochim. Acta. (2017). doi:10.1016/j.electacta.2017.05.150.

[56]   G. Godillot, L. Guerlou-Demourgues, P.-L. Taberna, P. Simon, C. Delmas, Original Conductive Nano-Co3O4 Investigated as Electrode Material for Hybrid Supercapacitors, Electrochem. Solid-State Lett. 14 (2011) A139. doi:10.1149/1.3609259.

[57]   D.Y. Momodu, F. Barzegar, A. Bello, J. Dangbegnon, T. Masikhwa, J. Madito, N. Manyala, Simonkolleite-graphene foam composites and their superior electrochemical performance, Electrochim. Acta. 151 (2015) 591–598. doi:10.1016/j.electacta.2014.11.015.

[58]   H. Peng, Z. Mo, S. Liao, H. Liang, L. Yang, F. Luo, H. Song, Y. Zhong, B. Zhang, High Performance Fe- and N- Doped Carbon Catalyst with Graphene Structure for Oxygen Reduction, Sci. Rep. 3 (2013) 1765. doi:10.1038/srep01765.

[59]   N. Daems, X. Sheng, Y. Alvarez-Gallego, I.F.J. Vankelecom, P.P. Pescarmona, Iron-containing N-doped carbon electrocatalysts for the cogeneration of hydroxylamine and electricity in a H$_2$ –NO fuel cell, Green Chem. 18 (2016) 1547–1559. doi:10.1039/C5GC02197A.

[60]   X. Rui, H. Tan, Q. Yan, Nanostructured metal sulfides for energy storage, Nanoscale. 6 (2014) 9889. doi:10.1039/C4NR03057E.

[61] M. Dirican, M. Yanilmaz, X. Zhang, Free-standing polyaniline–porous carbon nanofiber electrodes for symmetric and asymmetric supercapacitors, RSC Adv. 4 (2014) 59427–59435. doi:10.1039/C4RA09103E.

[62] H. MI, X. ZHANG, S. AN, X. YE, S. YANG, Microwave-assisted synthesis and electrochemical capacitance of polyaniline/multi-wall carbon nanotubes composite, Electrochem. Commun. 9 (2007) 2859–2862. doi:10.1016/j.elecom.2007.10.013.

[63] S.K. Simotwo, C. Delre, V. Kalra, Supercapacitor Electrodes Based on High-Purity Electrospun Polyaniline and Polyaniline-Carbon Nanotube Nanofibers, ACS Appl. Mater. Interfaces. 8 (2016) 21261–21269. doi:10.1021/acsami.6b03463.

[64] M. Wu, G.A. Snook, V. Gupta, M. Shaffer, D.J. Fray, G.Z. Chen, Electrochemical fabrication and capacitance of composite films of carbon nanotubes and polyaniline, J. Mater. Chem. 15 (2005) 2297. doi:10.1039/b418835g.

[65] M.J. Bleda-Martínez, C. Peng, S. Zhang, G.Z. Chen, E. Morallón, D. Cazorla-Amorós, Electrochemical Methods to Enhance the Capacitance in Activated Carbon/Polyaniline Composites, J. Electrochem. Soc. 155 (2008) A672. doi:10.1149/1.2956969.

[66] D. Salinas-Torres, J.M. Sieben, D. Lozano-Castelló, D. Cazorla-Amorós, E. Morallón, Asymmetric hybrid capacitors based on activated carbon and activated carbon fibre-PANI electrodes, Electrochim. Acta. 89 (2013) 326–333. doi:10.1016/j.electacta.2012.11.039.

[67] K.S. Ryu, Y.-G. Lee, K.M. Kim, Y.J. Park, Y.-S. Hong, X. Wu, M.G. Kang, N.-G. Park, R.Y. Song, J.M. Ko, Electrochemical capacitor with chemically polymerized conducting polymer based on activated carbon as hybrid electrodes, Synth. Met. 153 (2005) 89–92. doi:10.1016/j.synthmet.2005.07.167.

[68] F. Chen, P. Liu, Q. Zhao, Well-defined graphene/polyaniline flake composites for high performance supercapacitors, Electrochim. Acta. 76 (2012) 62–68. doi:10.1016/j.electacta.2012.04.154.

[69] G.A. Snook, P. Kao, A.S. Best, Conducting-polymer-based supercapacitor devices and electrodes, J. Power Sources. 196 (2010) 1–12. doi:10.1016/j.jpowsour.2010.06.084.

[70]   S. Bose, T. Kuila, A.K. Mishra, R. Rajasekar, N.H. Kim, J.H. Lee, Carbon-based nanostructured materials and their composites as supercapacitor electrodes, J. Mater. Chem. Mater. Chem. 22 (2012) 767–784. doi:10.1039/c1jm14468e.

[71]   Y. Zhou, H. Xu, N. Lachman, M. Ghaffari, S. Wu, Y. Liu, A. Ugur, K.K. Gleason, B.L. Wardle, Q.M. Zhang, Advanced asymmetric supercapacitor based on conducting polymer and aligned carbon nanotubes with controlled nanomorphology, Nano Energy. 9 (2014) 176–185.

[72]   W. Sun, X. Chen, Preparation and characterization of polypyrrole films for three-dimensional micro supercapacitor, 193 (2009) 924–929. doi:10.1016/j.jpowsour.2009.04.063.

[73]   H. Li, J. Wang, Q. Chu, Z. Wang, F. Zhang, S. Wang, Theoretical and experimental specific capacitance of polyaniline in sulfuric acid, 190 (2009) 578–586. doi:10.1016/j.jpowsour.2009.01.052.

[74]   T.M. Masikhwa, F. Barzegar, J.K. Dangbegnon, A. Bello, M.J. Madito, D. Momodu, N. Manyala, Asymmetric supercapacitor based on VS $_2$ nanosheets and activated carbon materials, RSC Adv. (2016). doi:10.1039/C5RA27155J.

[75]   P.L. Taberna, P. Simon, J.-F.F. Fauvarque, Electrochemical Characteristics and Impedance Spectroscopy Studies of Carbon-Carbon Supercapacitors, J. Electrochem. Soc. 150 (2003) A292-300. doi:10.1149/1.1543948.

[76]   L. Chen, H. Bai, Z. Huang, L. Li, Mechanism investigation and suppression of self-discharge in active electrolyte enhanced supercapacitors, Energy Environ. Sci. 7 (2014) 1750–1759. doi:10.1039/C4EE00002A.

[77]   F. Barzegar, A.A. Khaleed, F.U. Ugbo, K.O. Oyeniran, D.Y. Momodu, A. Bello, J.K. Dangbegnon, N. Manyala, F. Barzegar, A.A. Khaleed, F.U. Ugbo, K.O. Oyeniran, Cycling and floating performance of symmetric supercapacitor derived from coconut shell biomass Cycling and floating performance of symmetric supercapacitor derived from coconut shell biomass, 115306 (2016). doi:10.1063/1.4967348.